AAAS
Research
Volume 2020, Article ID 6591981, 10 pages
https://doi.org/10.34133/2020/6591981

Research
A SCIENCE PARTNER JOURNAL

Research Article

Crystalline Structure-Dependent Mechanical and Thermoelectric Performance in $Ag_2Se_{1-x}S_x$ System

Jiasheng Liang,[1,2] Pengfei Qiu,[1] Yuan Zhu,[3] Hui Huang,[1,2] Zhiqiang Gao,[1,2,4] Zhen Zhang,[3] Xun Shi,[1] and Lidong Chen[1,2]

[1]*State Key Laboratory of High Performance Ceramics and Superfine Microstructure, Shanghai Institute of Ceramics, Chinese Academy of Sciences, Shanghai 200050, China*
[2]*Center of Materials Science and Optoelectronics Engineering, University of Chinese Academy of Sciences, Beijing 100049, China*
[3]*Division of Solid-State Electronics, Department of Electrical Engineering, Uppsala University, Uppsala, Sweden*
[4]*School of Physical Science and Technology, ShanghaiTech University, Shanghai 201210, China*

Correspondence should be addressed to Pengfei Qiu; qiupf@mail.sic.ac.cn and Xun Shi; xshi@mail.sic.ac.cn

Received 21 April 2020; Accepted 17 June 2020; Published 31 July 2020

Self-powered wearable electronics require thermoelectric materials simultaneously with a high dimensionless figure of merit (zT) and good flexibility to convert the heat discharged by the human body into electricity. $Ag_2(S,Se)$-based semiconducting materials can well satisfy these requirements, and thus, they are attracting great attention in thermoelectric society recently. $Ag_2(S,Se)$ crystalizes in an orthorhombic structure or monoclinic structure, depending on the detailed S/Se atomic ratio, but the relationship between its crystalline structure and mechanical/thermoelectric performance is still unclear to date. In this study, a series of $Ag_2Se_{1-x}S_x$ ($x = 0$, 0.1, 0.2, 0.3, 0.4, and 0.45) samples were prepared and their mechanical and thermoelectric performance dependence on the crystalline structure was systematically investigated. $x = 0.3$ in the $Ag_2Se_{1-x}S_x$ system was found to be the transition boundary between orthorhombic and monoclinic structures. Mechanical property measurement shows that the orthorhombic $Ag_2Se_{1-x}S_x$ samples are brittle while the monoclinic $Ag_2Se_{1-x}S_x$ samples are ductile and flexible. In addition, the orthorhombic $Ag_2Se_{1-x}S_x$ samples show better electrical transport performance and higher zT than the monoclinic samples under a comparable carrier concentration, most likely due to their weaker electron-phonon interactions. This study sheds light on the further development of flexible inorganic TE materials.

1. Introduction

Recently, thermoelectric (TE) technology shows a great potential to be used as a sustainable power source in wearable electronics [1–3]. Via harvesting the heat discharged by the human body and converting it into electricity, the wearable electronics using TE technology can be self-powered without using any external batteries. The energy conversion efficiency of a TE material is determined by the dimensionless figure of merit, $zT = \alpha^2\sigma T/\kappa$, where α is the Seebeck coefficient, σ is the electrical conductivity, κ is the thermal conductivity, and T is the absolute temperature. The TE material used in wearable electronics should possess high zT to maximize the energy conversion efficiency and good flexibility to match the curved surface of skin and endure repeated bending during service [4–6].

To date, Bi_2Te_3-based alloys are still the best room-temperature TE materials, but their application in wearable electronics is limited due to their inherent brittleness [7–14]. In contrast, the organic TE polymers show good flexibility, but their zTs are low [15–20]. Recently, we reported a class of Ag_2S-based flexible inorganic TE materials with excellent intrinsic flexibility and high zTs [21]. Monoclinic Ag_2S shows surprisingly high ductility at room temperature due to its wrinkled layer structure (space group $P2_1/n$, with the sketch map shown in Figure 1(a), and weak Ag-S chemical bonds [22, 23]. However, its relatively wide band gap (around 1 eV) yields low σ only in the order of 10^{-1} S m^{-1}. As a result, zT of the stoichiometric Ag_2S around room temperature is very poor. Alloying Se or/and Te in Ag_2S can significantly improve σ and enhance zT to 0.26 for $Ag_2S_{0.5}Se_{0.5}$ and 0.44 for $Ag_2S_{0.5}Se_{0.45}Te_{0.05}$ at 300 K.

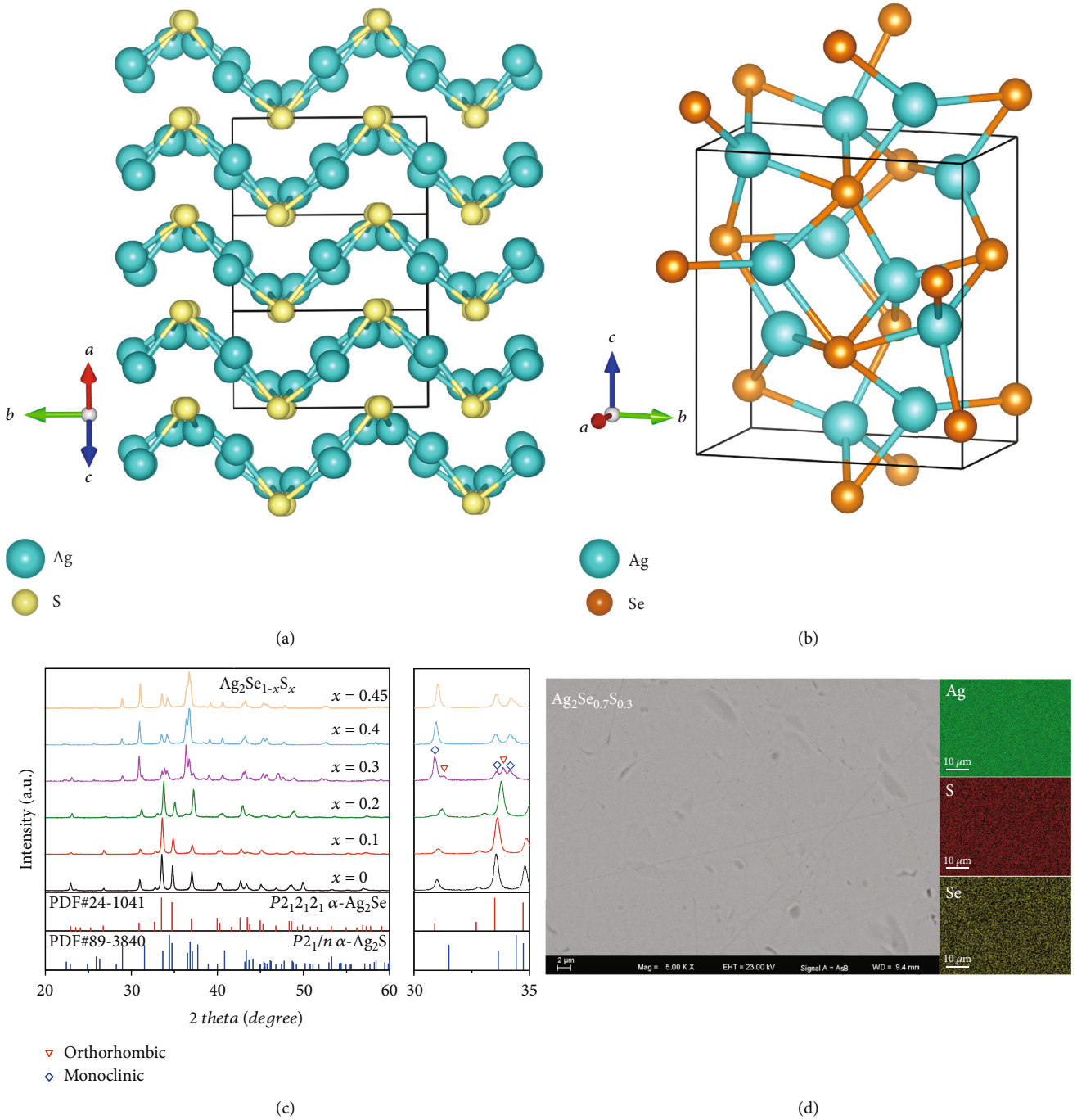

Figure 1: Crystalline structures for (a) monoclinic Ag_2S and (b) orthorhombic Ag_2Se. (c) Room-temperature X-ray diffraction patterns for $Ag_2Se_{1-x}S_x$ ($x = 0$, 0.1, 0.2, 0.3, 0.4, and 0.45) samples. The right panel shows the magnification around $2\theta = 30 \sim 35°$. (d) Backscatter electron (AsB) image and elemental energy dispersive spectroscopy (EDS) mappings of $Ag_2Se_{0.7}S_{0.3}$.

Particularly, previous study showed that the good ductility can be well maintained when the Se alloying content in Ag_2S reaches 50% or the Te alloying content reaches 20%, enabling these materials very suitable to be used in flexible wearable electronics. The above results arouse great interest on the Ag_2S-based materials in TE society [21, 23–25].

Being different with ductile Ag_2S, Ag_2Se is a brittle material. It adopts an orthorhombic structure (space group $P2_12_12_1$) with the sketch map shown in Figure 1(b). The band gap of orthorhombic Ag_2Se is around 0.2 eV, about one-fifth of that of monoclinic Ag_2S. Orthorhombic Ag_2Se has very high carrier mobility (~10^3 cm^{-2} V^{-1} S^{-1}), excellent σ (~10^5 S m^{-1}), and extremely low lattice thermal conductivity (~0.3-0.5 W m^{-1} K^{-1}), resulting in high zT about 0.4~1.0 at 300 K [26–32]. Despite the different crystalline structures of Ag_2S and Ag_2Se, Bindi and Pingitore [33] reported that Ag_2S and Ag_2Se can form a continuous solid solution. The room-temperature crystalline structure of $Ag_2S_{1-x}Se_x$ solid

solution is the same with the monoclinic Ag_2S when $x \leq 0.6$, but the same with the orthorhombic Ag_2Se when $x \geq 0.7$. Considering that the carrier concentration of Ag_2Se is about several orders of magnitude higher than that of Ag_2S [22], $Ag_2S_{1-x}Se_x$ solid solution might process continuous adjustable carrier concentrations and TE properties. The mechanical properties and TE performance of $Ag_2Se_{1-x}S_x$ ($0.5 \leq x \leq 1$) have been already reported previously [33], but those of $Ag_2Se_{1-x}S_x$ ($0 \leq x \leq 0.5$) have not been investigated yet. Particularly, the relationship between crystalline structure and mechanical/TE performance for $Ag_2Se_{1-x}S_x$ solid solution is still unclear so far.

In this study, a series of polycrystalline $Ag_2Se_{1-x}S_x$ ($x = 0$, 0.1, 0.2, 0.3, 0.4, and 0.45) samples were prepared. Their crystalline structures, mechanical properties, and TE properties were systematically investigated. $x = 0.3$ in the $Ag_2Se_{1-x}S_x$ system was identified to be the transition boundary of the orthorhombic structure and monoclinic structure. Orthorhombic $Ag_2Se_{1-x}S_x$ ($x = 0$, 0.1, and 0.2) samples are brittle, while monoclinic $Ag_2Se_{1-x}S_x$ ($x = 0.4$ and 0.45) are ductile and flexible. Due to the stronger electron-phonon interaction, monoclinic $Ag_2Se_{0.6}S_{0.4}$ has lower PF and zT than orthorhombic $Ag_2Se_{1-x}S_x$ ($x = 0$, 0.1, and 0.2). However, the superior TE performance and thermal stability to the organic TE materials and the intrinsically good flexibility still promise a great potential for monoclinic $Ag_2Se_{1-x}S_x$ to be used in wearable electronics.

2. Results and Discussion

Figure 1(c) shows the X-ray diffraction patterns for the prepared $Ag_2Se_{1-x}S_x$ ($x = 0$, 0.1, 0.2, 0.3, 0.4, and 0.45) obtained at room temperature. When the S content $x < 0.3$, the diffraction peaks are well indexed to the orthorhombic structure of Ag_2Se with the space group of $P2_12_12_1$. This indicates that $Ag_2Se_{0.9}S_{0.1}$ and $Ag_2Se_{0.8}S_{0.2}$ still adopt the same crystalline structure with Ag_2Se at room temperature. When $x = 0.4$ and 0.45, the diffraction peaks agree well with the monoclinic structure of Ag_2S phase with the space group of $P2_1/n$. Likewise, the $Ag_2Se_{1-x}S_x$ ($x \geq 0.5$) samples also crystalize in the same monoclinic structure of Ag_2S [21]. Elemental energy dispersive spectroscopy (EDS) mappings confirm that all elements are homogeneously distributed in $Ag_2Se_{0.9}S_{0.1}$, $Ag_2Se_{0.8}S_{0.2}$, $Ag_2Se_{0.6}S_{0.4}$, and $Ag_2Se_{0.55}S_{0.45}$. No obvious secondary phase is observed. Thus, these samples are phase pure. Likewise, scanning electron microscopy (SEM) performed on the cross-section of $Ag_2Se_{0.6}S_{0.4}$ indicates that it has an obvious layered structure (cf. Fig. S1).

One special composition in the $Ag_2Se_{1-x}S_x$ system is $Ag_2Se_{0.7}S_{0.3}$. As shown in Figure 1(c), its X-ray diffraction pattern looks like that of monoclinic $Ag_2Se_{0.6}S_{0.4}$. However, besides those belonging to the monoclinic structure, some extra diffraction peaks with weak intensities are also observed, such as (102) at $2\theta = 31^\circ$ and (112) at $2\theta = 34^\circ$ (right panel in Figure 1(c)). These are indexed to the orthorhombic structure. Thus, $Ag_2Se_{0.7}S_{0.3}$ is believed to be a mixture rather than a pure phase, in which the main phase crystalizes in the monoclinic structure while the secondary phase crystalizes in the orthorhombic structure. This result is different from that proposed by Bindi and Pingitore [33] that $Ag_2Se_{0.7}S_{0.3}$ crystalizes in the same orthorhombic structure with Ag_2Se. Figure 1(d) shows the EDS mappings performed on $Ag_2Se_{0.7}S_{0.3}$. Surprisingly, all elements are still homogeneously distributed. Thus, it is concluded that the two different phases in $Ag_2Se_{0.7}S_{0.3}$ have very similar chemical compositions but different crystalline structures. A similar polymorphic feature has been also observed in the $Cu_2Se_{1-x}S_x$ system [34]. Combining the above result, it can be concluded that the transition boundary between the monoclinic and orthorhombic structures in $Ag_2S_{1-x}Se_x$ solid solution should be around $x = 0.3$.

$Ag_2Se_{1-x}S_x$ ($x = 0$, 0.1, 0.2, 0.3, 0.4, and 0.45) samples possess structure-dependent mechanical properties. The three-point bending test and Vickers hardness test were performed on $Ag_2Se_{1-x}S_x$. The material with larger bending deformation or small Vickers hardness is usually a benefit for the application in flexible electronics [2, 3, 6]. Figure 2(a) shows that orthorhombic Ag_2Se can only endure a very small bending strain before cracking. The maximum bending deformation is about 0.56%. Likewise, orthorhombic $Ag_2Se_{0.9}S_{0.1}$ also possesses a maximum bending deformation around 1.5%. The case is different for monoclinic $Ag_2Se_{0.6}S_{0.4}$, which exhibits a bending deformation above 10% without cracking. Previously, large bending deformation was also observed for monoclinic $Ag_2Se_{1-x}S_x$ ($x = 0.5$, 0.7, 0.9, and 1) in the bending test. It should be noted that such deformation is plastic, which is different from the elastic deformation of brittle materials with low dimension. Likewise, Vickers hardness for orthorhombic Ag_2Se is 43.7 Hv at room temperature. It is monotonously increased to 51.5 Hv and 62.7 Hv for the orthorhombic $Ag_2Se_{0.9}S_{0.1}$ and $Ag_2Se_{0.8}S_{0.2}$, respectively. However, monoclinic $Ag_2Se_{0.6}S_{0.4}$ has low Vickers hardness of only 33.8 Hv, about half of that for orthorhombic $Ag_2Se_{0.8}S_{0.2}$. As shown in Figure 2(c), $Ag_2Se_{0.6}S_{0.4}$ can be directly cut into thin strips with thickness about 0.1 mm like metal. Furthermore, these metal-like strips can be twisted into various shapes without cracking, confirming that $Ag_2Se_{0.6}S_{0.4}$ has good ductility and flexibility.

The above test results prove that the monoclinic structure has significantly better ductility and flexibility in the $Ag_2Se_{1-x}S_x$ system. The high cleavage energy and low slipping energy, related to the unique wrinkled layer structure, are the fundamental reason for the good ductility observed in monoclinic $Ag_2Se_{1-x}S_x$. Previous investigation found that the S atoms in monoclinic Ag_2S always bonded to part of the surrounding Ag atoms during slipping [22, 35], which is benefit for preventing the material's cleavage under mechanical stress. Likewise, it enables the bonding energy between Ag and S atoms to change fluently, yielding a low energy barrier for slipping. However, in the orthorhombic structure, such unique wrinkled layer structure does not exist; thus, the orthorhombic $Ag_2Se_{1-x}S_x$ samples are brittle. Here, it should be noted that although the main phase in $Ag_2Se_{0.7}S_{0.3}$ crystalizes in the monoclinic structure, $Ag_2Se_{0.7}S_{0.3}$ still has low maximum bending deformation around 0.88%. The reason should be attributed to the presence of brittle orthorhombic grains

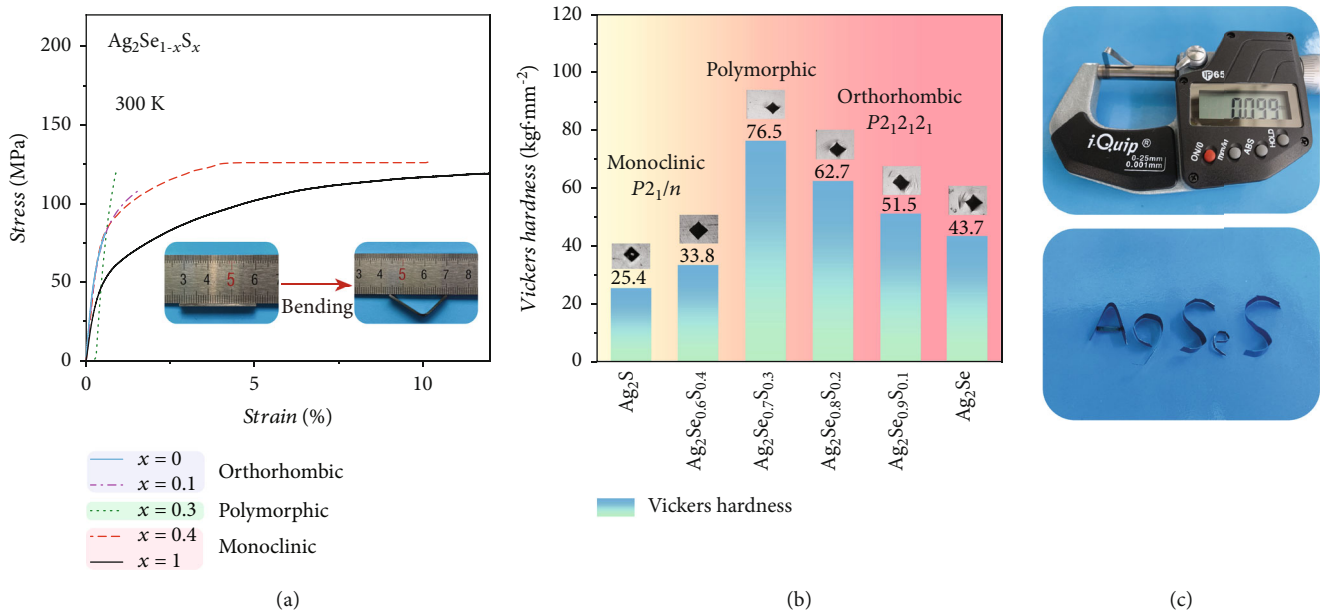

FIGURE 2: (a) Strain-stress curves for the three-point bending test of $Ag_2Se_{1-x}S_x$ ($x = 0$, 0.1, 0.3, and 0.4) samples at 300 K. The tests were performed by using a dynamic mechanical analyzer (DMA). The insets show the optical images of $Ag_2Se_{0.6}S_{0.4}$ sample before and after the bending test. The data for Ag_2S are included for comparison [22]. (b) Vickers hardness of $Ag_2Se_{1-x}S_x$ under the load of 0.3 kgf. The insets are micrographs of indention. Vickers hardness of Ag_2S reported in Ref. 22 is included for comparison. (c) $Ag_2Se_{0.6}S_{0.4}$ strips twisted into various shapes. The thickness of $Ag_2Se_{0.6}S_{0.4}$ strips is 0.1 mm.

among the ductile monoclinic grains. The second phase strengthening effect caused by these brittle orthorhombic grains will impede the movement of atoms, dislocations, or interfaces under mechanical stress like that in the pure orthorhombic phase, yielding poor ductility for $Ag_2Se_{0.7}S_{0.3}$.

Figure 3 shows the measured σ and α for $Ag_2Se_{1-x}S_x$ ($x = 0$, 0.1, 0.2, 0.3, 0.4, and 0.45). All samples possess negative α, indicating that they are n-type semiconductors with electrons dominating the electrical transports. This scenario is the same with those $Ag_2Se_{1-x}S_x$ ($x \geq 0.5$) samples. Obvious σ and α discontinuous jumps are observed between 360 K and 420 K, which are attributed to the orthorhombic-cubic or monoclinic-cubic phase transition. For example, Ag_2Se experiences orthorhombic-cubic phase transition around 410 K. At 300 K, σ for Ag_2Se is about 1.4×10^5 S·m^{-1}. It increases with increasing temperature, reaching around 3.1×10^5 S·m^{-1} at 403 K, and then decreases to 1.9×10^5 S·m^{-1} after the phase transition. The σ value for $Ag_2Se_{0.55}S_{0.45}$ at 300 K is only 3.6×10^4 S·m^{-1}, almost one-fourth of the pristine Ag_2Se. Likewise, the α values vary from -146 μV·K^{-1} to -105 μV·K^{-1} at 300 K and from -45 μV·K^{-1} to -109 μV·K^{-1} at 420 K, without obvious chemical composition dependence. Furthermore, Fig. S2 shows that the prepared samples have good reproducibility. When the chemical composition and fabrication process are fixed, different batches of samples have comparable σ and α data.

With the purpose to understand the electrical transport properties of $Ag_2Se_{1-x}S_x$, Hall measurements were performed. The Hall carrier concentration (n_H) and mobility (μ_H) at 300 K are listed in Table SI. All $Ag_2Se_{1-x}S_x$ samples possess n_H in the order of 10^{18} cm^{-3}. However, being similar with the above measured σ and α, the n_H values do not have monotonous variation with the sulfur content. The different contents of intrinsic defects inside the lattice, such as Ag interstitials, are expected to be the reason for this scenario. Likewise, the μ_H values for the $Ag_2Se_{1-x}S_x$ samples are in the range of 309 cm^2·V^{-1}·s^{-1} to 1337 cm^2·V^{-1}·s^{-1}. These μ_H values are quite high as compared with other state-of-the-art TE materials, such as 190 cm^2·V^{-1}·s^{-1} for n-type Bi_2Te_3 [36] and 48 cm^2·V^{-1}·s^{-1} for n-type filled skutterudites [37]. A single parabolic model (SPB) is used to further understand the electrical transports of $Ag_2Se_{1-x}S_x$. According to the SPB model, the Seebeck coefficient, carrier concentration, and carrier mobility can be correlated as follows [38–40]:

$$\alpha = \frac{\kappa_B}{e}\left[\frac{(2+\lambda)F_{\lambda+1}(\eta)}{(1+\lambda)F_\lambda(\eta)} - \eta\right], \quad (1)$$

$$n_H = 4\pi\left(\frac{2m^* k_B T}{h^2}\right)^{3/2}\frac{F_{1/2}(\eta)}{r_H}, \quad (2)$$

$$\mu_H = \frac{3\sqrt{\pi}}{4}\frac{(1/2)+2\lambda}{1+\lambda}\frac{1}{\Gamma(2+\lambda)}\frac{F_{2\lambda-1/2}}{F_\lambda}\mu_{ph}, \quad (3)$$

$$\mu_{ph} = \frac{(8\pi)^{1/2}e\hbar^4\rho v_l^2}{3(k_B T)^{3/2}(m^*)^{5/2}\Xi^2}, \quad (4)$$

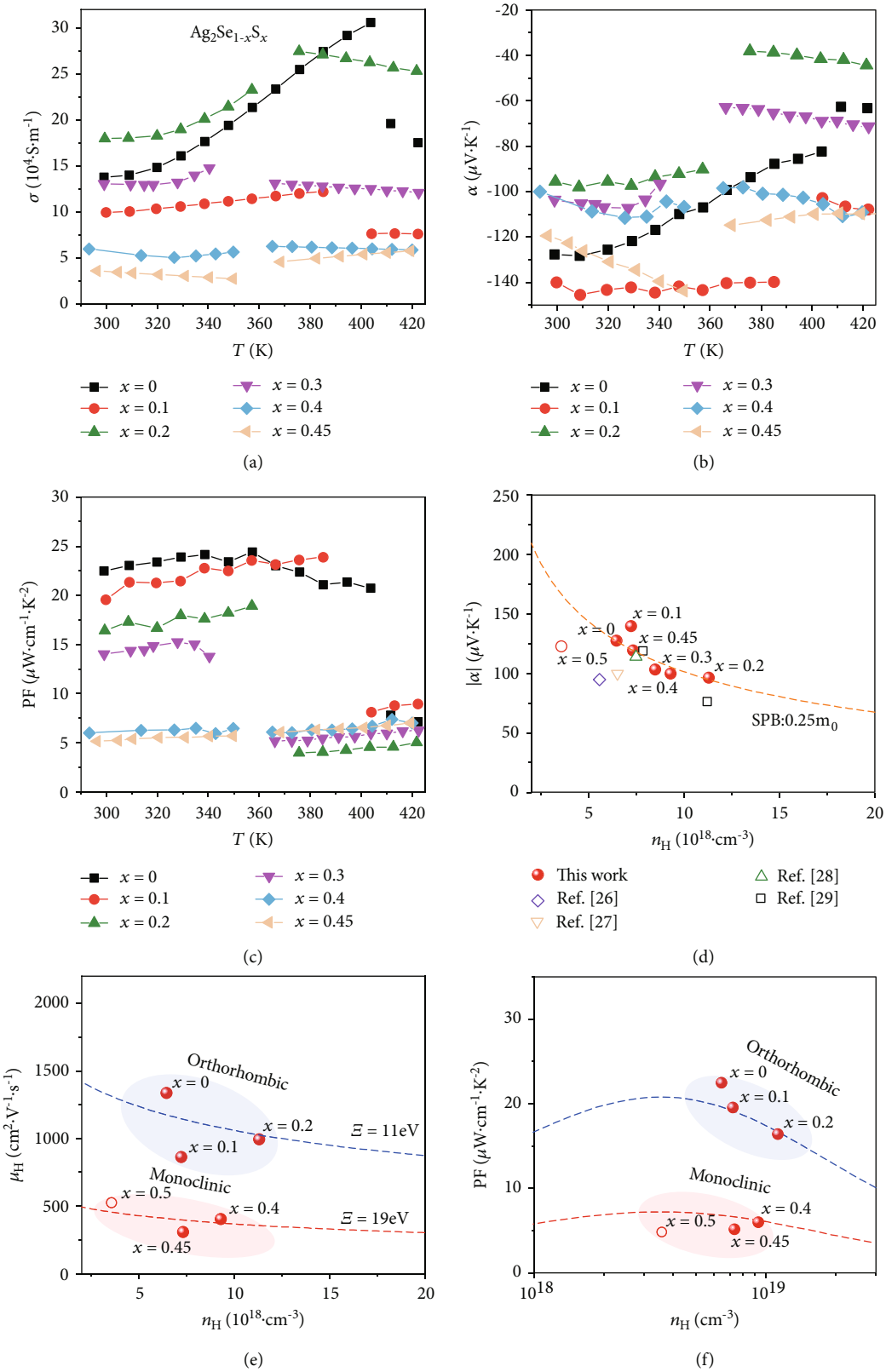

FIGURE 3: Temperature dependences of (a) electrical conductivity σ and (b) Seebeck coefficient α for $Ag_2Se_{1-x}S_x$ ($x = 0$, 0.1, 0.2, 0.3, 0.4, and 0.45). (c) Temperature dependence of power factor (PF) for $Ag_2Se_{1-x}S_x$ ($x = 0$, 0.1, 0.2, 0.3, 0.4, and 0.45). (d) Seebeck coefficient α, (e) Hall carrier mobility μ_H, and (f) PF as a function of carrier concentration n_H for $Ag_2Se_{1-x}S_x$ at 300 K. The dashed lines represent the theoretical curves based on the single parabolic band (SPB) model with a dominated scattering mechanism by acoustic phonons. The data for Ag_2Se and $Ag_2Se_{0.5}S_{0.5}$ reported before are added for comparison [21, 26–29].

$$r_H = \frac{3}{4}\frac{F_{1/2}(\eta)F_{-1/2}(\eta)}{F_0{}^2(\eta)}, \quad (5)$$

where k_B is the Boltzmann constant, λ is the scattering factor, e is the electron charge, m^* is the density-of-state effective mass, r_H is the Hall factor, ρ is the sample density, v_l is the velocity of longitudinal sound waves, μ_{ph} is the drift mobility for acoustic phonon scattering in the nondegenerate limit, and Ξ is the deformation potential. $F_m(\eta)$ is the Fermi integrals, and it is given by equation $F_m(\eta) = \int_0^\infty x^m dx/(1 + e^{x-\eta})$, where x represents the reduced carrier energy and $\eta = E_F/k_BT$ is the reduced Fermi energy.

Figure 3(d) presents that the α and n_H data for the present $Ag_2Se_{1-x}S_x$ ($x = 0$, 0.1, 0.2, 0.3, 0.4, and 0.45) samples roughly fall around the calculated theoretical Pisarenko curve with $m^* = 0.25m_e$ (m_e is the mass of free electron) and $\lambda = 0$ (acoustic phonon scattering). For comparison, the previously reported data for Ag_2Se and $Ag_2Se_{0.5}S_{0.5}$ are also summarized in Figure 3(d). These data also fall around the theoretical curve. This scenario suggests that all these samples might possess a similar band structure near the Fermi level, despite the fact that some of them crystalize in the monoclinic structure while others in the orthorhombic structure. This is possible because the conduction band minimums of Ag_2S and Ag_2Se are at the same gamma point and both of them are mainly dominated by Ag-5s electrons [21, 41]. Alloying S at the Se sites would mainly alter the valence band maximum instead of the conduction band minimum, yielding the similar m^* mentioned above. In addition, the small m^*, about $0.25m_e$ for these $Ag_2(S,Se)$ samples, are responsible for their higher μ_H than those for n-type Bi_2Te_3 [36] and filled skutterudites [37] mentioned above.

Figure 3(e) plots the μ_H and n_H relationship at 300 K for $Ag_2Se_{1-x}S_x$ ($x = 0$, 0.1, 0.2, 0.4, 0.45, and 0.5). The data for $Ag_2Se_{0.7}S_{0.3}$ are not included because its polymorphic feature might introduce extra boundary scattering to electrons and interrupt the understanding on the carrier mobility. As shown in Figure 3(e), under the similar n_H, the $Ag_2Se_{1-x}S_x$ ($x = 0$, 0.1, and 0.2) samples with an orthorhombic structure have higher μ_H than the $Ag_2Se_{1-x}S_x$ ($x = 0.4$, 0.45, and 0.5) samples with a monoclinic structure. By fitting the experimental data of the μ_H and n_H relationship using Equations (1)–(5), deformation potential values of 11 eV and 19 eV can be extracted for the orthorhombic $Ag_2Se_{1-x}S_x$ ($x = 0$, 0.1, and 0.2) and the monoclinic $Ag_2Se_{1-x}S_x$ (0.4, 0.45, and 0.5), respectively. The thermal vibrations of the crystal lattice can influence the energy-band structure and perturb the carrier transports. The intensity of such interaction between electrons and phonons can be reflected by the magnitude of Ξ [42]. The lower Ξ value for the orthorhombic $Ag_2Se_{1-x}S_x$ suggests that the electron-phonon interaction wherein is weaker than that in the monoclinic $Ag_2Se_{1-x}S_x$. This is responsible for the higher μ_H observed for the orthorhombic $Ag_2Se_{1-x}S_x$.

The power factors (PF) for $Ag_2Se_{1-x}S_x$ ($x = 0$, 0.1, 0.2, 0.3, 0.4, and 0.45) samples calculated from the formula $PF = \alpha^2 \cdot \sigma$ are shown in Figure 3(c). At 300 K, the PF value for Ag_2Se reaches 22.5 $\mu W \cdot cm^{-1} \cdot K^{-2}$. It gradually decreases with increasing the S-alloying content. At 300 K, the PF for $Ag_2Se_{0.55}S_{0.45}$ is just 5.2 $\mu W \cdot cm^{-1} \cdot K^{-2}$, about one-fourth of that for Ag_2Se. The greatly reduced σ is responsible for the lowered PF. The PF value for $Ag_2Se_{0.6}S_{0.4}$ is comparable with that for $Ag_2Se_{0.5}S_{0.5}$ reported before [21, 24], about 4.8 $\mu W \cdot cm^{-1} \cdot K^{-2}$ at 300 K. Based on the SPB model, the theoretical PF vs. n_H curves at 300 K can be obtained for the orthorhombic and monoclinic $Ag_2Se_{1-x}S_x$ samples, respectively. As shown in Figure 3(f), the experimental PF and n_H data basically fall around these lines. Under the comparable n_H, the PF for the orthorhombic $Ag_2Se_{1-x}S_x$ samples are much higher than those of the monoclinic $Ag_2Se_{1-x}S_x$ samples. The reason is that the orthorhombic samples have weaker electron-phonon interaction than the monoclinic samples, which yields lower Ξ value for higher μ_H and PF. In addition, based on the SPB model, the optimal carrier concentration ($n_{opt,PF}$) corresponding to the peak PF is around $3\text{-}4 \times 10^{18}$ cm^{-3} for both orthorhombic and monoclinic $Ag_2Se_{1-x}S_x$. n_H for the present orthorhombic $Ag_2Se_{1-x}S_x$ ($x = 0$, 0.1, and 0.2) and monoclinic $Ag_2Se_{1-x}S_x$ ($x = 0.4$) samples are already close to this $n_{opt,PF}$ value.

Figure 4(a) shows κ as a function of temperature for $Ag_2Se_{1-x}S_x$ ($x = 0$, 0.1, 0.2, 0.3, 0.4, and 0.45). The discontinuous jumps on the κ curves are attributed to the orthorhombic-cubic or monoclinic-cubic phase transitions. κ ranges from 0.7 $W \cdot m^{-1} \cdot K^{-1}$ to 1.4 $W \cdot m^{-1} \cdot K^{-1}$ for all samples. $Ag_2Se_{0.6}S_{0.4}$ exhibits the lowest κ among all samples. κ for $Ag_2Se_{0.6}S_{0.4}$ at 300 K is around 0.7 $W \cdot m^{-1} \cdot K^{-1}$. This value is about 36% decrement as compared with that for $Ag_2Se_{0.8}S_{0.2}$. Generally, κ is composed of two parts: the electron part κ_e and the lattice part κ_L. κ_e can be calculated according to the Wiedemann-Franz law [43]. Figure 4(b) shows the calculated κ_e/κ for $Ag_2Se_{1-x}S_x$ ($x = 0$, 0.1, 0.2, 0.3, 0.4, and 0.45). It can be seen that the κ_e/κ values are in the range of 48% to 80%, indicating that the carriers' contribution is very important in the thermal transports. By subtracting κ_e from κ, κ_L can be obtained. The results at 300 K are listed in Table SI. They range from 0.20 $W \cdot m^{-1} \cdot K^{-1}$ to 0.48 $W \cdot m^{-1} \cdot K^{-1}$, which are very low values as compared with those for the state-of-the-art TE materials [44–49]. The proximity to the cubic superionic phase is responsible for the low κ_L values observed in these orthorhombic and monoclinic phases [23].

Based on the measured α, σ, and κ, zT can be calculated according to $zT = \alpha^2\sigma T/\kappa.zT$ for orthorhombic Ag_2Se is around 0.6 in the whole measured temperature range, which is comparable with those reported before [28–30]. Orthorhombic $Ag_2Se_{0.9}S_{0.1}$ and $Ag_2Se_{0.8}S_{0.2}$ possess comparable zTs with Ag_2Se. However, zTs for monoclinic $Ag_2Se_{0.6}S_{0.4}$ and $Ag_2Se_{0.55}S_{0.45}$ are much lower than those for orthorhombic Ag_2Se. At 300 K, zT is just 0.26 for $Ag_2Se_{0.6}S_{0.4}$ and 0.23 for $Ag_2Se_{0.55}S_{0.45}$.

As shown in Figure 4(d), the theoretical zT vs. n_H curves for orthorhombic and monoclinic $Ag_2Se_{1-x}S_x$ samples at 300 K are given by assuming that all samples possess the same $\kappa_L = 0.4$ $W\,m^{-1}\,K^{-1}$. The experimental zT and n_H data basically fall around these lines. Under the comparable n_H, zT for the orthorhombic $Ag_2Se_{1-x}S_x$ samples is much higher than that of the monoclinic $Ag_2Se_{1-x}S_x$ samples because their

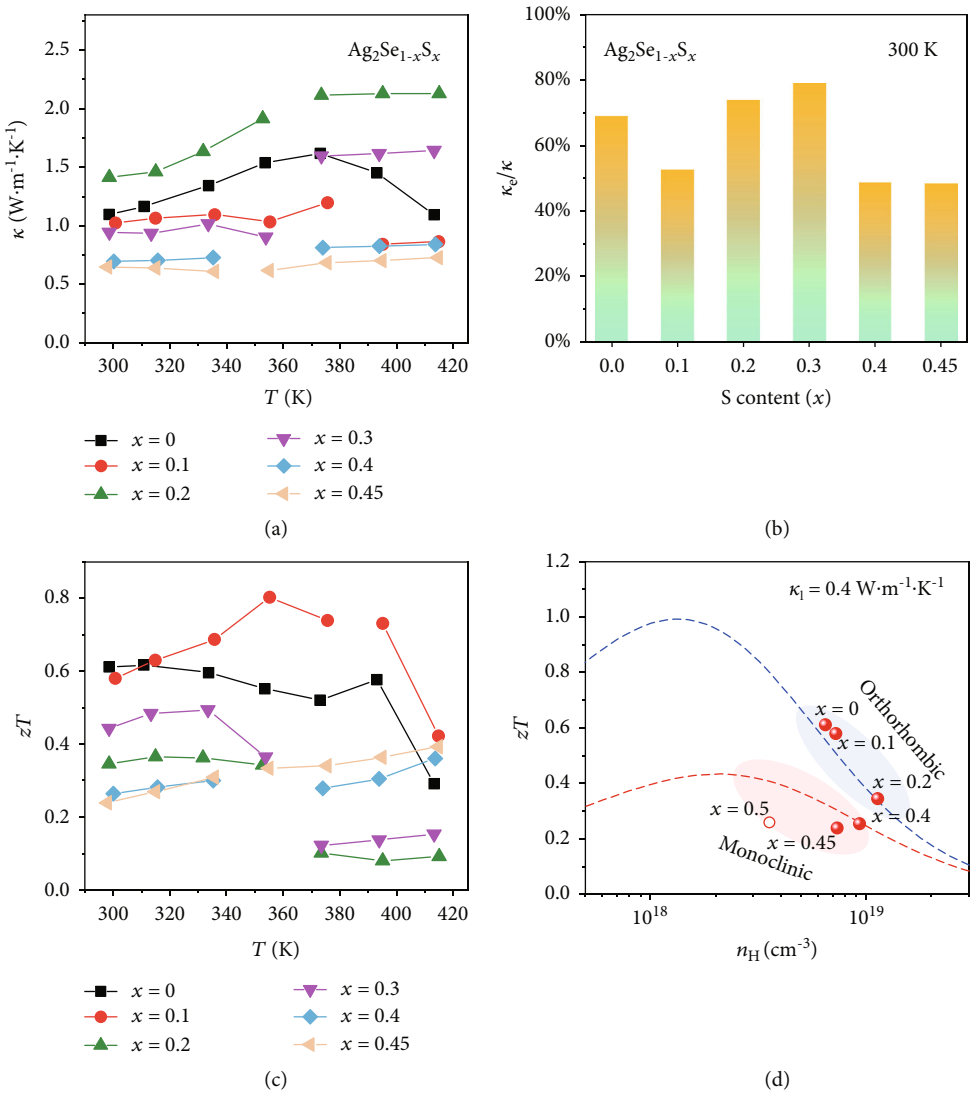

FIGURE 4: (a) Temperature dependence of thermal conductivity for $Ag_2Se_{1-x}S_x$ ($x = 0$, 0.1, 0.2, 0.3, 0.4, and 0.45). (b) The ratio of electronic thermal conductivity to thermal conductivity (κ_e/κ) at 300 K for $Ag_2Se_{1-x}S_x$. (c) Temperature dependence of TE figure of merit zT for $Ag_2Se_{1-x}S_x$ ($x = 0$, 0.1, 0.2, 0.3, 0.4, and 0.45). (d) zT as a function of carrier concentration n_H for $Ag_2Se_{1-x}S_x$ at 300 K. The dashed lines represent the theoretical curves based on the single parabolic band (SPB) model. The data for $Ag_2Se_{0.5}S_{0.5}$ reported before are added for comparison.

weaker electron-phonon interaction yields lower Ξ value and larger μ_H for higher PF. The optimal carrier concentration ($n_{opt,zT}$) corresponding to the peak zT is around $1\text{-}2 \times 10^{18}$ cm^{-3} for orthorhombic $Ag_2Se_{1-x}S_x$, while $2\text{-}3 \times 10^{18}$ cm^{-3} for monoclinic $Ag_2Se_{1-x}S_x$. n_H for the present orthorhombic $Ag_2Se_{1-x}S_x$ ($x = 0$, 0.1, and 0.2) and monoclinic $Ag_2Se_{1-x}S_x$ ($x = 0.4$, 0.45, and 0.5) samples are still higher than these $n_{opt,zT}$ values. Thus, if their carrier concentration can be further reduced, higher zT can be expected.

Although the TE performances for ductile monoclinic $Ag_2Se_{1-x}S_x$ are lower than those for brittle orthorhombic $Ag_2Se_{1-x}S_x$, their performances are still much higher than those for the organic TE materials reported before. This can be clearly reflected by the scenario shown in Figure 5. The PF values for most of the n-type TE organic TE materials are lower than 1 $\mu W \cdot cm^{-1} \cdot K^{-2}$ at 300 K. Even for the best n-type TE organic TE materials reported so far, poly(Ni-ett) [19], its PF, 3.6 $\mu W \cdot cm^{-1} \cdot K^{-2}$ at 300 K, is still lower than the present monoclinic $Ag_2Se_{1-x}S_x$. The superior PF values achieved in the monoclinic $Ag_2Se_{1-x}S_x$ samples would promise high power output when they are fabricated into TE devices. In addition, most n-type organic TE materials are unstable in the air because their electron affinity is too low to stabilize the n-type dopants [2, 50]. In contrast, the present ductile monoclinic $Ag_2Se_{1-x}S_x$ samples are inert to oxygen or water; thus, they can realize good service stability in real application. Combining the intrinsically good flexibility and ductility, these monoclinic $Ag_2Se_{1-x}S_x$ samples show great potential to be used in wearable electronics.

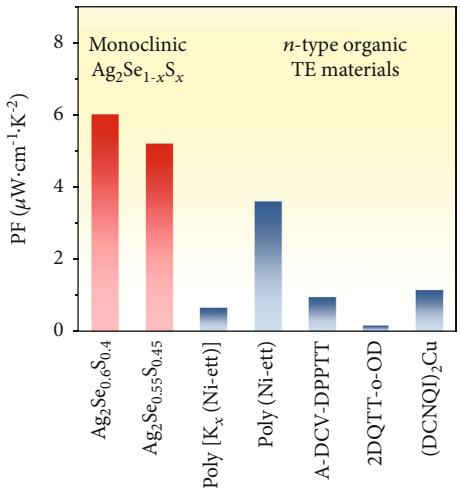

FIGURE 5: Comparisons of power factor values for *n*-type monoclinic $Ag_2Se_{1-x}S_x$ and *n*-type organic TE materials reported before [16, 19, 51–53].

3. Conclusion

In summary, this study systematically studied the crystalline structure, mechanical properties, and TE properties of $Ag_2Se_{1-x}S_x$ ($x = 0$, 0.1, 0.2, 0.3, 0.4, and 0.45). $Ag_2Se_{1-x}S_x$ samples crystalize in the orthorhombic structure when $x \leq 0.2$, while in the monoclinic structure when $x \geq 0.4$. Only the monoclinic $Ag_2Se_{1-x}S_x$ samples possess good ductility and flexibility. Under comparable carrier concentration range, the orthorhombic $Ag_2Se_{1-x}S_x$ samples have higher carrier mobility, larger power factor, and better zT than the monoclinic samples because they have weaker electron-phonon interaction. This leads to lower zT values of monoclinic $Ag_2Se_{1-x}S_x$ ($x = 0.4$ and 0.45) samples than those of the orthorhombic $Ag_2Se_{1-x}S_x$ ($x = 0.1$ and 0.2) samples. However, the higher PF and better thermal stability promise a great potential for monoclinic $Ag_2Se_{1-x}S_x$ to be used in wearable electronics.

Conflicts of Interest

The authors declare no competing financial interests.

Authors' Contributions

P.Q., X.S., and L.C. conceived the idea. J.L. conducted the synthesis, TE transport property measurement, and bending test. Z.G. and H.H. conducted the Hall measurement and Vickers hardness measurements. J.L, P.Q., Y.Z. and Z.Z. contributed to data analysis, model interpretation, and paper drafting. J.L., P.Q., and X.S. completed the writing of the manuscript. All authors discussed the results and gave comments regarding the manuscript.

Acknowledgments

This work is supported by the National Key Research and Development Program of China (2018YFB0703600) and the National Natural Science Foundation of China (51625205, 91963208, and 5181101519). X.S. thanks the support by the CAS-DOE Program of Chinese Academy of Sciences under Grant No. 121631KYSB20180060. P.Q. thanks the support by the Youth Innovation Promotion Association of CAS under Grant No. 2016232 and Shanghai Rising-Star Program under Grant No. 19QA1410200. This work is also partially supported by the Swedish Research Council (VR) via the Sweden-China collaborative project 2018-06030.

Supplementary Materials

Materials and methods. Fig. S1: cross-section image of $Ag_2Se_{0.6}S_{0.4}$ bulk sample. Fig. S2: electrical properties for three batches of $Ag_2Se_{0.8}S_{0.2}$ and $Ag_2Se_{0.6}S_{0.4}$. Table SI: room-temperature thermoelectric properties of $Ag_2Se_{1-x}S_x$ samples. *(Supplementary Materials)*

References

[1] H. Jin, J. Li, J. Iocozzia et al., "Hybrid organic–inorganic thermoelectric materials and devices," *Angewandte Chemie International Edition*, vol. 58, no. 43, pp. 15206–15226, 2019.

[2] Y. Wang, L. Yang, X. L. Shi et al., "Flexible thermoelectric materials and generators: challenges and innovations," *Advanced Materials*, vol. 31, no. 29, article 1807916, 2019.

[3] J. C. Yang, J. Mun, S. Y. Kwon, S. Park, Z. Bao, and S. Park, "Electronic skin: recent progress and future prospects for skin-attachable devices for health monitoring, robotics, and prosthetics," *Advanced Materials*, vol. 31, no. 48, article e1904765, 2019.

[4] Y. Jiang and B. Tian, "Inorganic semiconductor biointerfaces," *Nature Reviews Materials*, vol. 3, no. 12, pp. 473–490, 2018.

[5] H. Yao, Z. Fan, H. Cheng et al., "Recent development of thermoelectric polymers and composites," *Macromolecular Rapid Communications*, vol. 39, no. 6, article e1700727, 2018.

[6] H. R. Lim, H. S. Kim, R. Qazi, Y. T. Kwon, J. W. Jeong, and W. H. Yeo, "Advanced soft materials, sensor integrations, and applications of wearable flexible hybrid electronics in healthcare, energy, and environment," *Advanced Materials*, vol. 32, no. 15, article e1901924, 2020.

[7] G. J. Snyder, J. R. Lim, C.-K. Huang, and J.-P. Fleurial, "Thermoelectric microdevice fabricated by a MEMS-like electrochemical process," *Nature Materials*, vol. 2, no. 8, pp. 528–531, 2003.

[8] S. J. Kim, J. H. We, and B. J. Cho, "A wearable thermoelectric generator fabricated on a glass fabric," *Energy & Environmental Science*, vol. 7, no. 6, pp. 1959–1965, 2014.

[9] S. J. Kim, H. E. Lee, H. Choi et al., "High-performance flexible thermoelectric power generator using laser multiscanning lift-off process," *ACS Nano*, vol. 10, no. 12, pp. 10851–10857, 2016.

[10] K. Nan, S. D. Kang, K. Li et al., "Compliant and stretchable thermoelectric coils for energy harvesting in miniature flexible devices," *Science Advances*, vol. 4, no. 11, article eaau5849, 2018.

[11] F. Kim, B. Kwon, Y. Eom et al., "3D printing of shape-conformable thermoelectric materials using all- inorganic Bi_2Te_3-based inks," *Nature Energy*, vol. 3, no. 4, pp. 301–309, 2018.

[12] R. Feng, F. Tang, N. Zhang, and X. Wang, "Flexible, high-power density, wearable thermoelectric nanogenerator and

self-powered temperature sensor," *ACS Applied Materials & Interfaces*, vol. 11, no. 42, pp. 38616–38624, 2019.

[13] Y. Pan, Y. Qiu, I. Witting et al., "Synergistic modulation of mobility and thermal conductivity in $(Bi,Sb)_2$ Te_3 towards high thermoelectric performance," *Energy & Environmental Science*, vol. 12, no. 2, pp. 624–630, 2019.

[14] J. Qiu, Y. Yan, T. Luo et al., "3D printing of highly textured bulk thermoelectric materials: mechanically robust BiSbTe alloys with superior performance," *Energy & Environmental Science*, vol. 12, no. 10, pp. 3106–3117, 2019.

[15] O. Bubnova, Z. U. Khan, A. Malti et al., "Optimization of the thermoelectric figure of merit in the conducting polymer poly(3,4-ethylenedioxythiophene)," *Nature Materials*, vol. 10, no. 6, pp. 429–433, 2011.

[16] Y. Sun, P. Sheng, C. di et al., "Organic thermoelectric materials and devices based on *p*- and *n*-type poly(metal 1,1,2,2-ethenetetrathiolate)s," *Advanced Materials*, vol. 24, no. 7, pp. 932–937, 2012.

[17] G. H. Kim, L. Shao, K. Zhang, and K. P. Pipe, "Engineered doping of organic semiconductors for enhanced thermoelectric efficiency," *Nature Materials*, vol. 12, no. 8, pp. 719–723, 2013.

[18] Q. Zhang, Y. Sun, W. Xu, and D. Zhu, "What to expect from conducting polymers on the playground of thermoelectricity: lessons learned from four high-mobility polymeric semiconductors," *Macromolecules*, vol. 47, no. 2, pp. 609–615, 2014.

[19] Y. Sun, L. Qiu, L. Tang et al., "Flexible n-type high-performance thermoelectric thin films of poly(nickel-ethylenetetrathiolate) prepared by an electrochemical method," *Advanced Materials*, vol. 28, no. 17, pp. 3351–3358, 2016.

[20] Q. Zhang, Y. Sun, Y. Qin, W. Xu, and D. Zhu, "Two soluble polymers with lower ionization potentials: doping and thermoelectric properties," *Journal of Materials Chemistry A*, vol. 4, no. 4, pp. 1432–1439, 2016.

[21] J. Liang, T. Wang, P. Qiu et al., "Flexible thermoelectrics: from silver chalcogenides to full-inorganic devices," *Energy & Environmental Science*, vol. 12, no. 10, pp. 2983–2990, 2019.

[22] X. Shi, H. Chen, F. Hao et al., "Room-temperature ductile inorganic semiconductor," *Nature Materials*, vol. 17, no. 5, pp. 421–426, 2018.

[23] W. Tuo, C. Hong-Yi, Q. Peng-Fei, S. Xun, and C. Li-Dong, "Thermoelectric properties of Ag_2S superionic conductor with intrinsically low lattice thermal conductivity," *Acta Physica Sinica*, vol. 68, no. 9, article 90201, 2019.

[24] T. Wang, K. Zhao, P. Qiu, Q. Song, L. Chen, and X. Shi, "Aguilarite Ag_4SSe thermoelectric material: natural mineral with low lattice thermal conductivity," *ACS Applied Materials & Interfaces*, vol. 11, no. 13, pp. 12632–12638, 2019.

[25] S. He, Y. Li, L. Liu et al., "Semiconductor glass with superior flexibility and high room temperature thermoelectric performance," *Science Advances*, vol. 6, no. 15, article eaaz8423, 2020.

[26] C. Lee, Y.-H. Park, and H. Hashimoto, "Effect of nonstoichiometry on the thermoelectric properties of a Ag_2Se alloy prepared by a mechanical alloying process," *Journal of Applied Physics*, vol. 101, no. 2, article 024920, 2007.

[27] F. F. Aliev, M. B. Jafarov, and V. I. Eminova, "Thermoelectric figure of merit of Ag_2Se with Ag and Se excess," *Semiconductors*, vol. 43, no. 8, pp. 977–979, 2009.

[28] T. Day, F. Drymiotis, T. Zhang et al., "Evaluating the potential for high thermoelectric efficiency of silver selenide," *Journal of Materials Chemistry C*, vol. 1, no. 45, pp. 7568–7573, 2013.

[29] W. Mi, P. Qiu, T. Zhang, Y. Lv, X. Shi, and L. Chen, "Thermoelectric transport of Se-rich Ag_2Se in normal phases and phase transitions," *Applied Physics Letters*, vol. 104, no. 13, article 133903, 2014.

[30] D. Yang, X. Su, F. Meng et al., "Facile room temperature solventless synthesis of high thermoelectric performance Ag_2Se via a dissociative adsorption reaction," *Journal of Materials Chemistry A*, vol. 5, no. 44, pp. 23243–23251, 2017.

[31] Y. Ding, Y. Qiu, K. Cai et al., "High performance n-type Ag_2Se film on nylon membrane for flexible thermoelectric power generator," *Nature Communications*, vol. 10, no. 1, p. 841, 2019.

[32] Y. Lu, Y. Qiu, K. Cai et al., "Ultrahigh power factor and flexible silver selenide-based composite film for thermoelectric devices," *Energy & Environmental Science*, vol. 13, no. 4, pp. 1240–1249, 2020.

[33] L. Bindi and N. E. Pingitore, "On the symmetry and crystal structure of aguilarite, Ag_4SeS," *Mineralogical Magazine*, vol. 77, no. 1, pp. 21–31, 2013.

[34] K. Zhao, A. B. Blichfeld, E. Eikeland et al., "Extremely low thermal conductivity and high thermoelectric performance in liquid-like $Cu_2Se_{1-x}S_x$ polymorphic materials," *Journal of Materials Chemistry A*, vol. 5, no. 34, pp. 18148–18156, 2017.

[35] G. Li, Q. An, S. I. Morozov et al., "Ductile deformation mechanism in semiconductor α-Ag_2S," *npj Computational Materials*, vol. 4, no. 1, 2018.

[36] F. Hao, T. Xing, P. Qiu et al., "Enhanced thermoelectric performance in n-type Bi_2Te_3-based alloys via suppressing intrinsic excitation," *ACS Applied Materials & Interfaces*, vol. 10, no. 25, pp. 21372–21380, 2018.

[37] X. Shi, J. Yang, J. R. Salvador et al., "Multiple-filled skutterudites: high thermoelectric figure of merit through separately optimizing electrical and thermal transports," *Journal of the American Chemical Society*, vol. 133, no. 20, pp. 7837–7846, 2011.

[38] H. J. Goldsmid, *Introduction to Thermoelectricity*, vol. 121, Springer, Berlin, 2010.

[39] H. Xie, H. Wang, Y. Pei et al., "Beneficial contribution of alloy disorder to electron and phonon transport in half-Heusler thermoelectric materials," *Advanced Functional Materials*, vol. 23, no. 41, pp. 5123–5130, 2013.

[40] K. Zhao, A. B. Blichfeld, H. Chen et al., "Enhanced thermoelectric performance through tuning bonding energy in $Cu_2Se_{1-x}S_x$ Liquid-like materials," *Chemistry of Materials*, vol. 29, no. 15, pp. 6367–6377, 2017.

[41] C. M. Fang, R. A. de Groot, and G. A. Wiegers, "Ab initio band structure calculations of the low-temperature phases of Ag_2Se, Ag_2Te and Ag_3AuSe_2," *Journal of Physics and Chemistry of Solids*, vol. 63, no. 3, pp. 457–464, 2002.

[42] G. S. Nolas, J. Sharp, and J. Goldsmid, *Thermoelectrics: Basic Principles and New Materials Developments*, vol. 45, Springer Science & Business Media, 2013.

[43] H. S. Kim, Z. M. Gibbs, Y. Tang, H. Wang, and G. J. Snyder, "Characterization of Lorenz number with Seebeck coefficient measurement," *APL Materials*, vol. 3, no. 4, 2015.

[44] J. Shuai, B. Ge, J. Mao, S. Song, Y. Wang, and Z. Ren, "Significant role of Mg stoichiometry in designing high thermoelectric performance for $Mg_3(Sb,Bi)_2$-based n-type Zintls," *Journal of the American Chemical Society*, vol. 140, no. 5, pp. 1910–1915, 2018.

[45] Z. Liu, J. Mao, J. Sui, and Z. Ren, "High thermoelectric performance of α-MgAgSb for power generation," *Energy & Environmental Science*, vol. 11, no. 1, pp. 23–44, 2018.

[46] Z. Chen, X. Zhang, and Y. Pei, "Manipulation of phonon transport in thermoelectrics," *Advanced Materials*, vol. 30, no. 17, article e1705617, 2018.

[47] T. Fu, J. Xin, T. Zhu, J. Shen, T. Fang, and X. Zhao, "Approaching the minimum lattice thermal conductivity of *p*-type SnTe thermoelectric materials by Sb and Mg alloying," *Science Bulletin*, vol. 64, no. 14, pp. 1024–1030, 2019.

[48] C. Chang and L.-D. Zhao, "Anharmoncity and low thermal conductivity in thermoelectrics," *Materials Today Physics*, vol. 4, pp. 50–57, 2018.

[49] T. Wang, Y. Xiong, Y. Wang et al., "Cu_3ErTe_3: a new promising thermoelectric material predicated by high-throughput screening," *Materials Today Physics*, vol. 12, article 100180, 2020.

[50] S. Wang, H. Sun, U. Ail et al., "Thermoelectric properties of solution-processed n-doped ladder-type conducting polymers," *Advanced Materials*, vol. 28, no. 48, pp. 10764–10771, 2016.

[51] D. Huang, H. Yao, Y. Cui et al., "Conjugated-backbone effect of organic small molecules for *n*-type thermoelectric materials with ZT over 0.2," *Journal of the American Chemical Society*, vol. 139, no. 37, pp. 13013–13023, 2017.

[52] F. Huewe, A. Steeger, K. Kostova et al., "Low-cost and sustainable organic thermoelectrics based on low-dimensional molecular metals," *Advanced Materials*, vol. 29, no. 13, article 1605682, 2017.

[53] D. Yuan, D. Huang, C. Zhang et al., "Efficient solution-processed n-type small-molecule thermoelectric materials achieved by precisely regulating energy level of organic dopants," *ACS Applied Materials & Interfaces*, vol. 9, no. 34, pp. 28795–28801, 2017.